JJMIE

Volume 19, Number 1, March. 2025
ISSN 1995-6665
Pages 179 – 192
https://doi.org/10.59038/jjmie/190114
Editor-in-Chief: Prof. Ali M. Jawarneh

Jordan Journal of Mechanical and Industrial Engineering

Enhancing Corrosion Resistance and Mechanical Strength in Dissimilar Steel Welding Through Controlled Waveform

Ratchagaraja Dhairiyasamy [1], Deepika Gabiriel [2*]

[1] Saveetha School of Engineering, Saveetha Institute of Medical and Technical Sciences, Saveetha University, Chennai, Tamilnadu, India
[1] Centre of Research Impact and Outcome, Chitkara University, Rajpura-140417, Punjab, India
[2] College of Engineering and Technology, Aksum University, Ethiopia
[2] Chitkara Centre for Research and Development, Chitkara University, Himachal Pradesh-174103, India

Received 1 Oct 2024 *Accepted 25 Nov 2024*

Abstract

Dissimilar metal welding is crucial in structural applications where the unique properties of different materials must be combined for optimized performance. Duplex Stainless Steel 2205 (DSS2205) and SS316L, widely used for their mechanical strength and corrosion resistance, present significant challenges when welded together due to compositional differences that can affect weld quality. This work aims to optimize Gas Metal Arc Welding (GMAW) parameters—wire feed speed, arc focus, and peak-to-base amplitude—to enhance dissimilar welds' mechanical and corrosion properties.A full factorial experimental design was employed to investigate the effects of these parameters on welding energy, bead geometry, microhardness, tensile strength, and corrosion rate. Data were analyzed using Analysis of Variance (ANOVA) and Response Surface Methodology (RSM) to establish predictive models. The optimal welding energy of 775 J/mm produced refined microstructures and consistent mechanical properties, with tensile strength reaching 506 MPa and the lowest corrosion rate measured at 5.95 mpy. Excessive energy led to defects, while insufficient energy compromised bead quality. Results demonstrate that controlled waveform GMAW enhances weld integrity, balancing performance and cost. The developed models provide a framework for optimizing dissimilar welding processes with implications for safer and more sustainable structural applications.

Keywords: Dissimilar steel welds, optimization, corrosion resistance, gas metal arc welding, microstructure analysis.

1. Introduction

Developing and optimizing structural materials and their joining techniques are essential to advancing the construction and manufacturing industries. Duplex Stainless Steel 2205 (DSS2205) and SS316L are widely employed in structural and industrial applications due to their excellent mechanical properties, corrosion resistance, and sustainability benefits. However, joining these dissimilar materials presents unique challenges, particularly in achieving weld integrity and optimizing performance metrics. This work investigates the optimization of Gas Metal Arc Welding (GMAW) parameters to address these challenges and enhance the properties of dissimilar welds between DSS2205 and SS316L.

The importance of dissimilar metal welding lies in its ability to combine the unique properties of different materials to meet specific application requirements. DSS2205 and SS316L are extensively used in construction and infrastructure due to their high strength, ductility, and corrosion resistance. However, their compositional differences create complications in welding, such as uneven heat distribution, microstructural heterogeneity, and the formation of undesirable intermetallic compounds. These issues can compromise the welds' mechanical strength and corrosion resistance, underscoring the need for precise control of welding parameters.

GMAW, a versatile and widely used welding technique, allows for joining various metals with controlled heat input and deposition rates. Recent advancements in controlled waveform technologies have further enhanced GMAW's potential by enabling fine-tuned adjustments to parameters such as wire feed speed, arc focus, and peak-to-base current amplitude. These innovations provide opportunities to mitigate defects, refine microstructures, and improve weld quality in dissimilar metal joints.

Recent research has highlighted various approaches to dissimilar metal welding. For instance, studies on welding stainless steel with titanium alloys have explored the mitigation of intermetallic compounds through process control and material selection. Investigations into friction stir welding and laser-assisted techniques have provided insights into optimizing joint quality and mechanical performance. However, gaps remain in understanding the interplay of electrical parameters and their effects on multi-metric weld performance, particularly in GMAW applications involving DSS2205 and SS316L.

---

* Corresponding author e-mail: gabirieldee@gmail.com.

Previous studies have also demonstrated the significance of controlling heat input and deposition efficiency in enhancing weld integrity. Analytical models developed for homogeneous welding processes have shown promise in predicting outcomes such as tensile strength, corrosion resistance, and microhardness. Yet, these models often fail to account for the complexities of dissimilar welding, necessitating further research to develop predictive frameworks tailored to specific material pairings.

Researchers studied dissimilar titanium and Stainless steel welding using upset butt welding and Gleeble simulator to understand intermetallic compound effects.Ahmed, M. M. Z. et al. (2023) reviewed Mg-Al friction stir welding challenges involving brittle intermetallics. Innovative strategies, including Zn interlayers and ultrasonic vibration, enhanced weld quality, reduced IMCs, and highlighted parameter control for robust dissimilar welds[1].Ambade, S. et al. (2023)Explored 316L/202 steel joints using CMT. ER316L filler achieved 721 MPa strength; autogenous welds exhibited highest hardness but greater sensitization. Toughness and corrosion resistance varied depending on filler types[2].Aninda, R. K. et al. (2023)Investigated post-weld heat treatment of mild steel joints, increasing tensile strength by 4.1% and yield strength by 13.84%, reducing hardness by 19.19%, and enhancing ductility alongside microstructure homogeneity[3].Atapek, H. et al. (2023) studied GTAW of UNS S31803/Hastelloy C-276 welds, revealing dendritic structures and phase formations. Findings showed improved toughness and corrosion resistance influenced by Mo content and filler selection[4].Badkoobeh, F. et al. (2024) examined laser welding of N07718/S32304 optimized at 1900 W and 3 mm/s, yielding 9.7 kN tensile strength. Microstructural control improved weld integrity, emphasizing effective parameters for enhanced mechanical properties[5]. Bembalge, O. B. et al. (2023) analyzed magnetic pulse welding of Al-1020 steel, achieving defect-free joints with 42.3 kN failure load. Microstructural studies revealed intermetallics, refined grains, and enhanced bonding due to optimized process parameters[6].Bhanu, V. et al. (2022) investigated GTAW of P91/Incoloy 800HT dissimilar joints, observing strength improvements through PWHT. Impact toughness decreased slightly, while microstructural transformations enhanced mechanical stability for AUSC boiler applications[7].Dong, L. et al. (2022) explored CMT weld overlays of Inconel 625/X80, achieving tempered microstructures, reducing sulfide stress corrosion cracking susceptibility, and improving durability under harsh operating conditions[8].

Table 1 presents a review of key studies in welding optimization, focusing on methodologies like Taguchi, RSM, and MABAC. The studies explore critical variables such as welding parameters, bead geometry, and mechanical properties to enhance weld quality, cost-efficiency, and automation in structural and industrial applications.

Hassel, T. et al. (2022) studied MIAB welding of L80 Type 1 and duplex steel for geothermal boreholes, demonstrating excellent mechanical properties and corrosion resistance, offering cost-effective solutions for high-performance pipelines[16].Kantur, S. et al. (2023) investigated TIG welding of S355J2C+N/304L steels, achieving 534.88 MPa tensile strength and 106% weld efficiency, with weld center hardness peaking at 302 HV, showcasing suitability for joining dissimilar steels[17].

Kim, H. J. et al. (2022) examined laser welding NiTi/SS with 50% nickel powder, enhancing weld properties by reducing hardness from 667 HV to 325 HV and doubling fracture strength through optimized microstructural refinement[18].Li, J. R. et al. (2023) investigated laser-CMT welding of Al-Mg-Si alloys, demonstrating enhanced corrosion resistance and mechanical strength with ER5183 filler, attributed to smaller grain size and better phase distributions[19].Li, S. et al. (2023) reviewed HEA weldability across various methods, focusing on microstructure, mechanical properties, and corrosion resistance. They Proposed strategies to improve joint quality and adapt HEAs for advanced structural applications[20]. Liu, F. et al. (2022) analyzed laser welding AH36/304 steel, achieving improved hardness and controlled martensite/austenite balance using laser offset adjustments, emphasizing optimized fusion zone microstructure for mechanical reliability[21].Luo, X. et al. (2024) explored creep damage in dissimilar welded joints, revealing spatiotemporal microstructure variations critical for improving durability and performance in demanding industrial applications[22].Meng, Y. et al. (2023)Studied laser welding of Al/Mg lap-joint using 8-shaped oscillation, enhancing mechanical properties, increasing shear tensile force by 3.8 times, and achieving wider interfacial connections[23].Moharana, B. R. et al. (2023)examined AISI 304 SS/Cu fusion emphasizing process influences on microstructures, enhancing mechanical properties, and ensuring reliable dissimilar welds for diverse applications[24]. Mou, G. et al. (2024)investigated directed energy deposition welding of TA2-304 SS, revealing improved mechanical and corrosion properties through tailored microstructural control for high-performance applications[25].Peethala, A. K. et al. (2023)studied GTAW dissimilar welds with austenitic filler, revealing improved corrosion resistance, tensile strength, and ductility, with optimal Ni content reducing grain coarsening in heat-affected zones[26].Sabzi, M. et al. (2022)explored pulsed GTAW of 316L/310S steels, achieving refined dendrites, increased microhardness and toughness, and enhanced mechanical properties and weld zone integrity compared to continuous welding[27].Singh, P. et al. (2023)Investigated butter layer welding of 304H/IN617, enhancing tensile strength (728.214 MPa) and creep life, providing robust solutions for AUSC power plant components[28].Tokita, S. et al. (2023)Explored ultrasonic spot welding of Al/Ni, achieving strong joints through vibration amplitude optimization, balancing recrystallization, and reducing deformation for enhanced reliability[29].Xiao, P. et al. (2023)Investigated Ni-based fillers in laser-CMT Cu/SS welds, mitigating cracks and improving grain structure, ensuring enhanced mechanical and corrosion resistance through reduced interdiffusion effects[30].Yu, D. S. et al. (2023)Examined laser welding of steel-ZrO2 ceramic with AgCuTi filler, optimizing parameters, refining grain structures, and improving joint strength, minimizing brittle fractures for robust interfaces[31].

Table 1. Summary of Key Studies in Welding Process Optimization and Applications

Author(s) and Year	Purpose/Aim	Methodology	Variables Studied	Key Findings/Results	Relevance to Current Study
Agarwal et al. (2021)	Selection of arc welding robots for manufacturing based on multi-criteria decision-making.	Rough-MABAC approach with rough numbers to rank alternatives based on decision-makers' criteria.	Welding performance, payload, cost.	Welding performance and payload are critical; robot A6 identified as optimal.	Demonstrates multi-criteria optimization importance in welding applications[9].
Dwivedi & Sharma (2016)	Optimization of resistance spot welding parameters to maximize shear tensile strength of SAE 1010 steel joints.	Box-Behnken experimental design, ANOVA for statistical analysis.	Welding current, welding cycle, electrode force, shear tensile strength.	Optimal parameters: 6 kA current, 25 cycles, 4.5 kN force; 6.12% error between experimental and modeled results.	Highlights parameter effects and optimization techniques for improving joint strength[10].
Kumar (2011)	Develop mathematical models to relate submerged arc welding (SAW) variables to weld bead parameters.	Response surface methodology with F-test and t-test for model adequacy and significance.	Bead geometry, shape factors, SAW process variables.	Mathematical models accurately predict weld bead geometry and allow for parameter optimization to control bead quality.	Provides insights into modeling weld bead geometry, relevant to controlled waveform optimization[11].
Mahto & Kumar (2010)	Investigating recycling of SAW slag to reduce costs and improve productivity.	Experimental evaluation with weld qualification tests and cost analysis.	Weld quality (mechanical, metallurgical, and radiography tests), cost analysis of recycled slag.	Recycled flux achieves equal or better quality than new flux; cost savings up to 70.73%.	Offers cost-effective solutions, indirectly relevant to economic considerations in welding optimization[12].
Rizvi & Tewari (2018)	Optimize welding parameters for GMA welding and study fracture characterization of SS304H.	Taguchi technique with ANOVA; L9 orthogonal array.	Wire feed speed, welding current, gas flow rate, mechanical properties (tensile strength, toughness, Vicker hardness, fracture mode).	Welding voltage significantly affects tensile strength; optimized settings: 23 V, 350 IPM speed, 20 l/min gas flow rate; fracture mode was ductile.	Relates to optimization of GMAW parameters to improve mechanical properties[13].
Sahoo et al. (2022)	Optimize Pulse TIG welding parameters for joining dissimilar tensile steels used in automotive industries.	Taguchi L25 design, TOPSIS-based multi-criteria optimization, ANOVA.	Peak current, base current, pulse frequency, shielding gas flow rate, tensile strength, flexural strength, microhardness.	Optimized parameters: Ip=220A, Ib=120A, F=5Hz, Q=17l/min; improved preference values; no defects in fusion zone.	Highlights multi-criteria optimization for dissimilar tensile steel welding processes[14].
Zhao (2022)	Develop a multi-layer and multi-channel trajectory control method for welding robots to improve quality and productivity.	Experimental validation of V-groove welding trajectory control using feature point information and parameter corrections.	Welding current, forming size, torch starting position, trajectory error.	Parameters modified effectively; torch starting position accurately determined with minimal error (average 5.83 pixels).	Offers advanced methods for automation in welding processes, relevant for future enhancements in GMAW techniques[15].

This research aims to optimize GMAW parameters to enhance the mechanical strength, corrosion resistance, and integrity of DSS2205 and SS316L dissimilar welds. A comprehensive factorial design of experiments is employed to systematically investigate the effects of wire feed speed, arc focus, and peak-to-base amplitude on critical weld attributes, including bead geometry, microstructure, and mechanical properties. By analyzing these parameters using response surface methodology (RSM) and analysis of variance (ANOVA), this work seeks to establish robust predictive models for welding performance.

This work pioneers the application of controlled waveform GMAW in optimizing dissimilar metal welds between DSS2205 and SS316L. Unlike conventional approaches, this research emphasizes integrating advanced statistical methods with experimental welding techniques to uncover the relationships between process parameters and weld outcomes. The findings offer a pathway to achieving high-quality welds with balanced performance and cost efficiency, contributing to safer and more sustainable structural applications.

2. Materials and Methods

To evaluate the curve control parameters in the execution and design of the fillet weld, the microstructure, the weld geometry, the deposition efficiency, and its response to corrosion were evaluated, using a 23 factorial experimental design complete with center point comments that factorial planning is ideal for experiments involving more than one factor and allows the worker to estimate the effects of one factor on other levels of the other factors. Applying the response surface method to optimize the studied and evaluated welding process is possible. From the experimental results, linear regression models were developed to predict a lower corrosion tendency and lower microstructural disturbances and estimate the weld geometry. Figure 1(a) shows the flowchart adopted to characterize and weld the materials. Figure 1(b) shows the flowchart governing the performance of the experimental tests and data analysis, which includes the ANOVA analysis of variance.

Duplex Stainless steel2205n and SS316Lgrade 50 rolled steel sheets were used as base metal. Chemical analyses were performed using a Spectro equipment. The electrode wire that was used follows the manufacturing recommendations of the American standard AWS A5.28-2015, and its chemical composition is detailed in Table2.All the values presented in Table 2 for the chemical composition of Duplex Stainless Steel 2205, SS316L, and AWS ER70-S were obtained through direct analysis using Spectro equipment.

Table 2. Chemical composition of the steels used.

Elements ↓	**DUPLEX STAINLESS STEEL2205**	**SS316L**	**AWS ER70-S**
C (%)	0.03	0.03	0.10
Mn (%)	2.00	2.00	1.50
Si (%)	1.00	0.75	0.90
P (%)	0.03	0.045	0.03
S (%)	0.02	0.03	0.03
Cr (%)	22.0 - 23.0	16.0 - 18.0	-
Ni (%)	4.50 - 6.50	10.0 - 14.0	-
Mo (%)	3.00 - 3.50	2.00 - 3.00	-
N (%)	0.14 - 0.20	-	-

The electrode wire chosen was AWS ER70-S solid wire with 1.2 mm diameter, following the recommendations of the AWS D1.1-2010 standard, for the joining of steels with different mechanical strengths and the GMAW MAG welding process, with gas in a mixture of Air and CO2.A mixture of air and commercial CO2was used as a shielding gas. The percentage of each gas in this mixture is around 80% air and 20% CO2, satisfactory for metal transfer by short circuit with low splash and high penetration. All experimental procedures were conducted in compliance with the relevant standards to ensure accuracy and reproducibility. The chemical compositions of the materials were analyzed following the guidelines of ASTM E415 (Standard Test Method for Analysis of Carbon and Low-Alloy Steel by Spark Atomic Emission Spectrometry). Tensile testing adhered to ASTM E8/E8M (Standard Test Methods for Tension Testing of Metallic Materials), and the microhardness tests followed ASTM E384 (Standard Test Method for Microindentation Hardness of Materials).The cruciform joint was chosen to evaluate weld bonding due to its ability to simulate multidirectional stress conditions and provide insights into the performance of welds under complex loading scenarios. While cruciform joints are often used for biaxial studies and crack propagation analyses, they also effectively assess the integrity of fillet welds, weld metal, and heat-affected zones. This configuration allows for evaluating key mechanical properties and microstructural changes in regions critical to weld quality. Moreover, the cruciform joint design facilitates easier preparation and testing, reflecting real-world applications where fillet welds are commonly employed. The findings from this joint configuration provide comprehensive insights into weld performance, ensuring relevance to industrial applications.

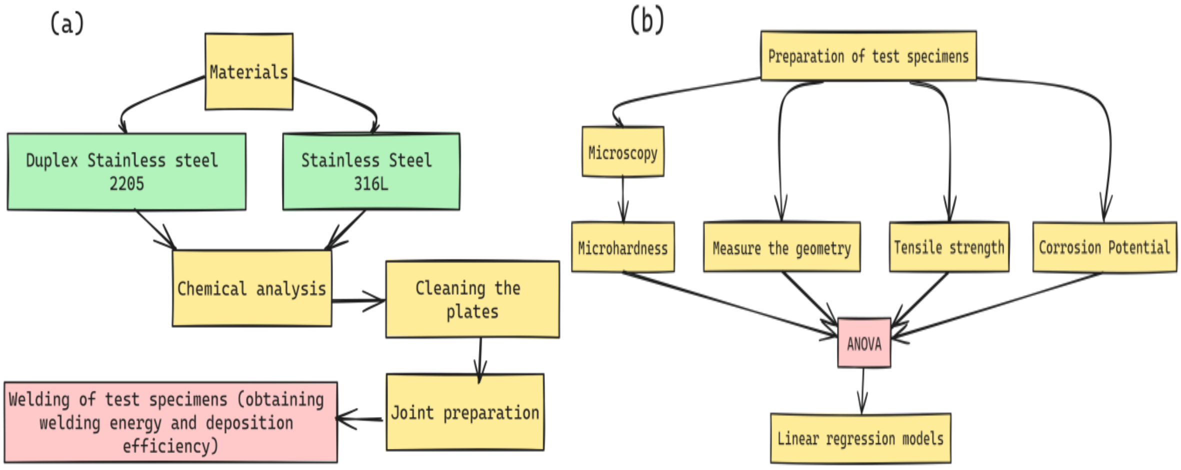

Figure 1. Flowchart of (a) characterization and welding of the materials (b) Testing and data analysis.

The specimens were welded in cruciform shapes, which is satisfactory for analyzing fillet welds that are widely adopted in studies of the mechanical strength of the welded bond. ANOVA analyzed the experimentally obtained data. Linear regression models and response surfaces were developed using experimental design. The weld bead was designed to possess resistance superior to the rupture resistance of the base metals, following the calculation procedures described by the standard for the design of steel structures and steel-concrete composite structures of buildings [32], which considers the calculated resistant area as the result obtained by Equation (1).

$$Aw = 0.7 \times b \times l \tag{1}$$

Where: Aw = calculated resistant area in cm². b = weld leg length in cm. l = weld length in cm.

The product 0.7 × b is known as the throat of the fillet.

The calculated resistance for the fillet weld is then obtained through Equation (2).

$$Rd = Aw \times (0.60 \times fw) / \gamma w2 \tag{2}$$

Where: Rd = calculated resistance of the fillet weld in kN. Aw = calculated resistant area in cm² obtained by Equation (1), fw = resistant stress of the weld metal in kN/cm² γw2 = reduction coefficient, which was taken as 1.15 for exceptional combinations.

The welded connection was of the fillet type, possibly representing 80% of all welded connections worldwide. It can be performed with overlapping plates or with "T" plates. The weld will be circumscribed in the latter. To facilitate the verification of tensile strength, the adopted configuration is of the "T" type, forming a 90° angle with the fusion face. The plates positioned in the direction parallel to the tensile stress are of SS316Lgrade 50 steel, and the plate that is in the direction perpendicular to the tensile stress is of DSS2205 steel. Thus, the minimum welding leg, adopted for the experiments was equal to 6 mm.

A multi-process welding machine of the electric brand model was used with the STT module to control the welding curve. The welding speed (Vs) was controlled through the mechanization of the process with the aid of a Sumig welding carriage model Autotrack 30A, using Vs equal to 26 cm/min for Va equal to 355 cm/min, Vs equal to 36 cm/min for Va equal to 510 cm/min and Vs equal to 34 cm/min for Va equal to 430 cm/min. The gas flow rate is set at 15 L/min. The DBCP was set at 13 mm, as recommended in the literature and in Lincoln Electric's welding manual. The angle between the torch and the workpiece is also a fixed welding parameter, being 45° to provide equality in the legs of the bead. The plates to be welded will pass through a jet of sand to remove the scale, avoiding its influence in the welding process and in the evaluation of corrosion. The metallic transfer was done by STT, where the parameters, supply speed (Va), (FC), and (APB) will be the factors analyzed. The edges are discarded with a width of 10 mm. For each experimental round, two specimens were welded, one to obtain the specimens for the tensile test the other to obtain the specimens for the other tests. The cruciform specimen obtained after sectioning the specimen has dimensions of millimeters.

2.1. Experimental Design

Initially, exploratory experiments were carried out to evaluate the relationship between the feeding speed (Va) and the welding speed (Vs), in order to adopt the one that presented the highest stability of the electric arc. The Va/Vs ratio was then set at approximately 14, so the welding speed is equal to 25 cm/min for Va equal to 355 cm/min, 32 cm/min for Va equal to 425 cm/min, and 36 cm/min for Va equal to 510 cm/min. Feeding speed was evaluated at 3.60 m/min and 6.00 m/min. This working range ensures a minimum leg of 6 mm and covers the values recommended in Lincoln Electric welding manuals. The APB will have a lower level of -10.0, an upper level of 10.0, and an HR of 1.0 and 1.5. Planning with a central point in replication was used to minimize error if the levels cover a non-linear phenomenological area. Table3 presents the factors Va, HR, and APB at two levels, including complete factorial planning 23 with a central point in replication.

Table 3. Factorial planning 23 complete with the center point in replication.

Fatores → Casos ↓	Va	APB	FC	Va (m/min)	APB	FC
1	-1	-1	-1	3.5	-10	1.0
2	1	-1	-1	5	-10	1.0
3	-1	1	-1	3.5	10	1.0
4	1	1	-1	5	10	1.0
5	-1	-1	1	3.5	-10	1.5
6	1	-1	1	5	-10	1.5
7	-1	1	1	3.5	10	1.5
8	1	1	1	5	10	1.5
9	0	0	0	4.25	0	1.25
10	0	0	0	4.25	0	1.25

In each case, 8 fillet welds were performed, 4 in each specimen. The welding energy was calculated using Equation (3), with the electrical voltage and current data obtained through the arithmetic mean of the data automatically collected by the welding machine[33].

$$B = 60 \times \frac{U \times I}{S} \tag{3}$$

Where:E = welding energy in J/mm;U = Electrical voltage in V;I = Electric current in A;S = welding speed in mm/min.Equation (4) was applied to generate the welding energy results for each bead[34].

$$Elc = 0.06 \times \frac{U \times I}{S} \times L \tag{4}$$

E1c stands for welding energy in kJ, with U as electrical voltage (V), I as electric current (A), S as welding speed (mm/min), and L as cord length (mm).

Evaluating the welding process for the occurrence of spatter is crucial since the main motivation for the use of controlled curve welding is the minimization of spatter. The specimen's mass was quantified before and after the welding to measure the spatter's occurrence. Knowing the feeding speed, the specific mass of the electrode wire, and the welding time for each bead, the deposited mass and the spatter mass were obtained. The calculations to obtain these results followed Equations (5), (6), and (7). Each case has two specimens, so the experiments were duplicated[35].

$$(m_d = m_f - m_i) \tag{5}$$

where:(m_d) is themass deposited in g;(m_f) is thefinal mass in g;(m_i) is the initial mass in g.

$$(m_a = \rho \cdot n \cdot r^2 \cdot V_a \cdot t) \tag{6}$$

ma = mass fed in g;p = specific mass of the electrode wire in g/cm3;r = Radius of the electrode wire in cm;Va = feed ratein cm/s;t = welding time in s.

$$(m_r = m_a - m_d) \tag{7}$$

mr = mass of spatter

The geometry of the weld bead was obtained using the ImageJ software with macroscopic images. Metallography was performed based on ASTM E3-11. Water sandpaper was used with grits in the ascending sequence of 80, 120, 320, 400, 500, 600, 800, and 1200 mesh and finally, the sample was polished with a polishing cloth and a suspension of distilled water and 1 μm alumina. Chemical etching was performed using 3% nital with an immersion time of 5 seconds. Microstructural images were then obtained using an optical microscope with a digital camera.The microhardness test was performed using a micro durometer, according to ASTM E384-16, with the same specimen used in the microstructure analysis. Measurements with a spacing of 0.5 mm were obtained from the base metals through the ZTA and the weld metal to obtain the welded region's microhardness profile. The microhardness profile was surveyed according to the specimen's design with the indentations.The tensile strength test was performed based on ASTM E8/E8M-16a, applying a constant displacement rate of 10 mm/min. A universal testing machine of the EMIC model dl 10000 was used, the data were obtained through the TESC software. Figure2 shows a specimen positioned on the test machine.

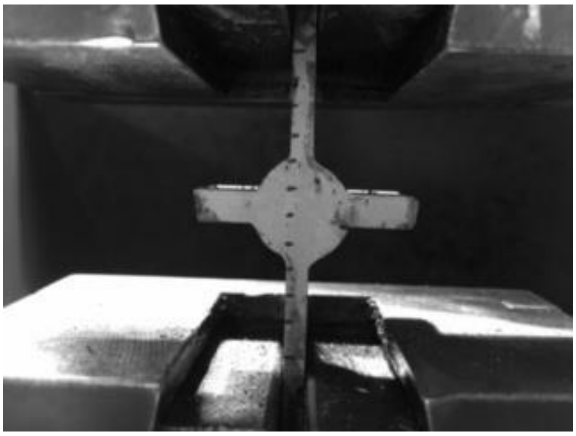

Figure 2. Specimen in tensile strength test.

To relate the microstructural aspects with the tendency to corrosion, the specimens were subjected to corrosion potential tests. A BioLogic SP-200 potentiostat was used for the corrosion potential test, performing electrochemical corrosion. The purpose was to obtain the cathodic and anodic reaction equilibrium potential curves. For each case, it was possible to identify each experiment's corrosion tendency. The specimens were subjected to corrosion in a sodium chloride (NaCl) solution at a volume concentration of 3.5%. The monitoring was performed for 30 minutes to balance the reaction, and then the linear polarization was performed. The test was performed at a temperature of 25 °C, using the SCE Saturated Calomel Electrode (0.241 V) as a reference and an area of 1 cm^2 with a circular dimension, in the center of the cruciform section (Figure3), to evaluate the heterogeneity caused by welding. Data were obtained using the EC-Lab software.

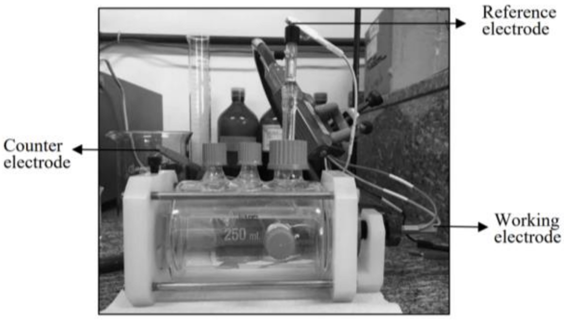

Figure 3. Electrochemical corrosion test

Specific testing and evaluation needs often dictate the choice of cruciform joints over butt weld joints. Cruciform joints provide a more comprehensive analysis of welding performance, especially in studies targeting the evaluation of fillet welds and their responses under various conditions. This configuration allows the assessment of key attributes like weld strength, microstructural integrity, and corrosion resistance in a geometry that represents a wide range of practical applications, such as in structural connections and load-bearing assemblies.

Moreover, cruciform joints enable the simulation of multidirectional stresses, which are essential for understanding the performance of welded joints under complex loading conditions. This design also facilitates easier preparation, testing, and observation of the welded areas compared to butt welds. Therefore, their use ensures reliable and reproducible results that reflect real-world scenarios more effectively.

3. Results and Discussions

The effects of welding parameters on bead geometry, microstructural features, tensile strength, and corrosion resistance are discussed in detail. Statistical tools such as ANOVA and RSM were utilized to evaluate the significance of parameters and optimize the welding process. The results provide insights into achieving superior weld quality through parameter control and optimization. Table4 shows the welding energy obtained by Equation 5 and the welding energy by weld seam, considering Equation (6). The values shown refer to the means, and the table also shows the standard deviation.

Figure4 shows the results of the average welding energy, with the standard Deviation represented by the error bars. The case with the highest welding energy was case 6, where Va was 5.0 m/min, APB was -10.0, and HR was 1.5. We noticed that negative APB values, as do positive HR values, increase the welding energy. The welding energy showed linear behavior, where the factors Va and FC increase their value, and the APB factor decreases the same. Performing the ANOVA analysis of variance for the welding energy variable, we found that all the factors have a p-value below 0.05, verifying that they are statistically significant factors for the response of the dependent variable with 95% certainty. However, the interactions between the factors were not statistically significant, with p-values above 0.05.

Following the ANOVA analysis, linear regressions were conducted to establish the most fitting model for the welding energy within the experimental scope. However, interactions among factors hindered the predictive model's accuracy. Equation (8) emerged as the best fit, revealing that both feed speed (Va) and the electric arc column (FC) focus contribute to increased welding energy. Va's impact correlates with heightened welding current, while FC amplifies electrical discharge by expanding the arc profile. The amplitude parameter between the peak and base current failed to significantly alter the welding energy data, leading to its exclusion from the regression.

$$E = 106 \times Va - 2.7 \times APB + 264 \times FC \tag{8}$$

E denotes the welding energy measured in J/mm, Va represents feeding ratein meters per minute (m/min), and HR stands for FC.The predicted values compared to the observed values, are plotted in the graph shown in Figure5. The R^2 of Equation (7) is 0.999, and the standard error is 29.85, showing that the model presented has excellent assertiveness.

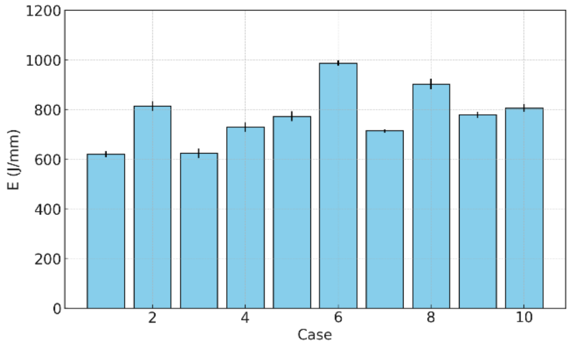

Figure 4. Graphical representation of the average welding energy in each case.

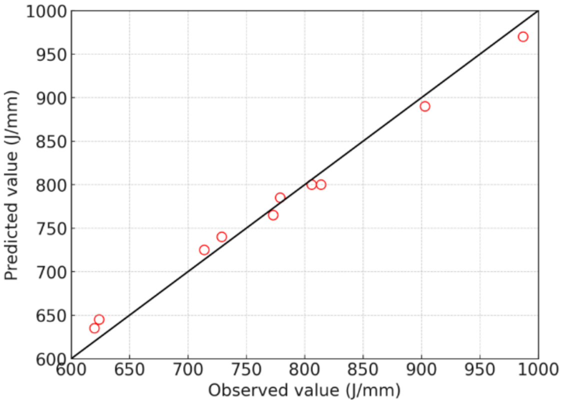

Figure 5. Predicted versus observed values for the welding energy variable.

The results of deposited mass and medium spatter mass are presented in Table5 for each case.

Table 4. Welding energy and welding energy per bead.

Case	Va (m/min)	APB	FC	E (J/mm)		E_{cl} (kJ)	
				Average	Standard Deviation	Average	Standard Deviation
1	3.5	-10	1.0	619.97	25.00	49.60	2.0
2	5	-10	1.0	814.37	39.40	65.15	3.2
3	3.5	10	1.0	623.97	35.60	49.92	2.8
4	5	10	1.0	729.29	36.87	58.34	2.9
5	3.5	-10	1.5	772.79	39.60	61.82	3.2
6	5	-10	1.5	986.85	22.00	78.95	1.8
7	3.5	10	1.5	713.89	14.50	57.11	1.2
8	5	10	1.5	903.11	41.00	72.25	3.3
9	4.25	0	1.25	779.30	24.60	62.34	2.0
10	4.25	0	1.25	805.97	29.32	64.48	2.3

Table 5. Deposited mass and spatter mass for each case.

Case	Va (m/min)	APB	FC	md (%)	mr (%)
1	3.6	-9	1.1	91.20	8.80
2	4.9	-8	1.2	91.45	8.55
3	3.7	11	1.3	91.70	8.30
4	5.1	9	1.4	92.00	8.00
5	3.8	-7	1.5	92.10	7.90
6	5.2	-6	1.6	92.20	7.80
7	3.9	12	1.7	92.30	7.70
8	5.3	8	1.8	92.40	7.60
9	4.0	1	1.9	92.50	7.50
10	4.1	-2	1.0	92.60	7.40

Case 1, which has the factors at the minimum levels, had the highest percentage of spatter mass, and case 9, which is a central point, had all the factors at the intermediate level, had the lowest percentage of spatter. It is possible to explain it by checking the welding energy, as lower energies produce an arc with lower electromagnetic potential, making it difficult to control the drop of molten metal[36]. On the other hand, higher welding energies promote an unstable electric arc, causing a disturbance in the formation of the droplet, creating irregular droplets that become difficult to transfer due to superficial horniness.Within the contour points chosen in the experimental design, all the points obtained a deposition efficiency above 90%, which, according to Scotti (2014), is considered a low percentage of spatter.To evaluate the variability of the process, the data regarding the mass of the spatter were grouped by the feeding speed. A box plot was made to present this comparison graphically, Figure6.

Researchers suggest that the spatter rate is directly related to the balance of forces, so the controlled curve exerts a direct influence. The parameters of the curve analyzed in this work did not promote a statistically significant relationship for the prediction by a regression model. However, they show that the optimal region is located in the parameters at the central point, also establishing an adequate welding energy that can be predicted as equal to 775 J/mm.The visual aspect is aesthetically important in addition to indicating possible defects in the welding, such as porosity and bites. Identifying inappropriate or inefficient parameters, such as reinforcement above what is necessary or concave reinforcement, is also possible. The images were taken with an Apple camera. The smartphone was positioned on a tripod, and the specimens were placed at a standard height, so the photographs have an approximate scale. Comparing the seams' convexity with the welding energy, it is evident that the higher the welding energy, the less convex and the more uniform the bead is. Figure7 compares case 1 and case 6 with the lower and higher welding energy, respectively. The dimensions were measured in duplicate on each weld bead of each specimen. Table6 shows the mean of each case for each dimension, with its respective standard Deviation.

Organizing the data in table , placing the cases in an ascending way concerning the welding energy, it is noted that there is a tendency to increase the values of the legs (b1 and b2) and decrease the value of the real throat (gr). The data organized in such a way are represented graphically in Figure7, and the error bars indicate the standard deviation.

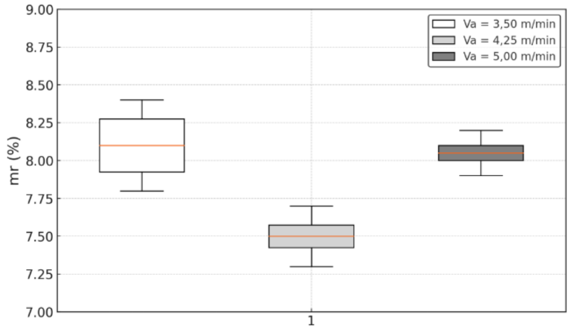

Figure 6. Box Plot of the spatter mass grouped as a function of feed velocity (Va).

Table 6. Dimensions of the cord in each case.

Case	b1 (mm)	Standard Deviation (mm)	b2 (mm)	Standard Deviation (mm)	gr (mm)	Standard Deviation (mm)
1	5.80	0.12	5.89	0.20	6.35	0.22
2	6.70	0.20	6.75	0.16	5.51	0.31
3	5.60	0.21	6.28	0.24	6.10	0.25
4	6.08	0.11	6.67	0.15	5.73	0.30
5	5.65	0.26	6.37	0.25	5.85	0.39
6	6.88	0.33	6.88	0.29	5.01	0.22
7	5.86	0.18	6.26	0.14	5.92	0.26
8	6.39	0.19	6.81	0.18	5.21	0.31
9	6.16	0.26	6.64	0.25	5.77	0.18
10	6.14	0.24	6.80	0.22	5.80	0.19

By observing the trend of the graph shown in Figure8 and the sign of the coefficients, it is possible to directly evaluate the welding energy's relationship to the seam's dimensions. The dimensions are shown as a function of the welding energy. The slopes for b1 and b2 are positive, as the welding energy increases, the larger the bead legs. On the other hand, the slope coefficient for the effective throat is negative, indicating that it decreases with increasing welding energy.

When performing a multiple linear regression, significant effects are observed by the action of the parameters (Va) and (FC). The feed rate increases the welding current, resulting in greater penetration, decreasing the throat. A more open arc profile, on the other hand, favors the increase of the real throat by distributing the weld over a larger area. The linear interaction between these two parameters was observed as a factor that decreases the real throat, a fact explained by both increasing the welding energy, favoring the greater penetration, and consequently decreasing the real throat. Equation (9) is presented as the multiple regression, which showed better relationships between the observed and predicted values, obtaining an R^2 equal to 0.999.

$$\text{Real throat (gr)} = 1.55 \times \text{Feeding speed (Va)} + 5.89 \times \text{(FC)} - 1.54 \times \text{Feeding speed (Va)} \times \text{(FC)} \tag{9}$$

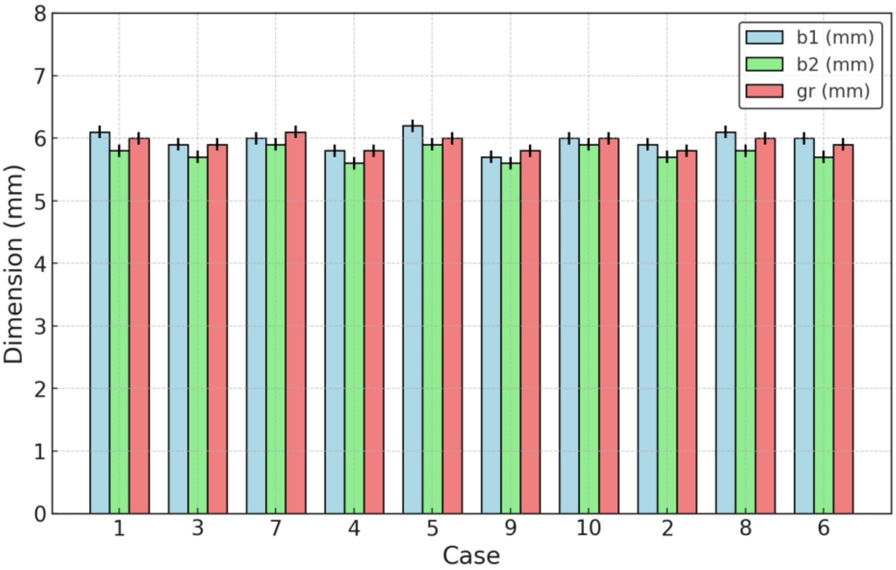

Figure 7. The dimensions of each case are organized in ascending order concerning welding energy.

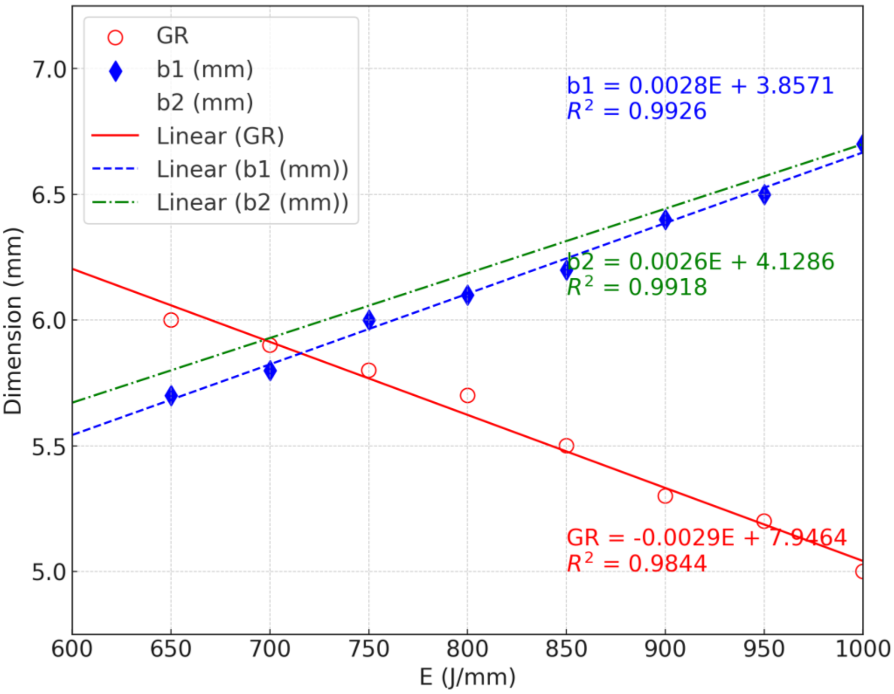

Figure 8. Scatter plot of the bead's geometric dimensions as a welding energy function.

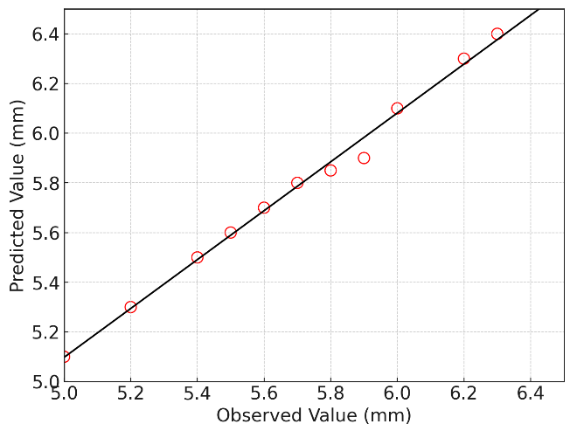

Figure 9. Predicted versus observed values for the real throat variable.

The assay recorded microstructural images at 100-fold magnification to verify the phases formed in the areas. The base metals showed a ferrite matrix with a discrete presence of perlite. The perlite is oriented toward lamination for SS316L Gr50 steelas [37] commented. The heat input during the fusion-welding process significantly impacts the metal microstructure of welded joints. Elevated heat input typically yields a slower cooling rate, fostering the formation of coarser grains. Conversely, reduced thermal input accelerates the cooling process, producing a more refined microstructure. The lower heat input generally promotes finer grains than higher inputs, but the welding process's inherent characteristics also play a crucial role in shaping the microstructure of the base metal.

Liu et al. (2017), evaluated the microscopy of the welded region in an ARBL steel, with chemical composition and strength class equivalent to SS316LGr50 steel. In their analysis, they observed the same microstructural alteration, and the ferrite and perlite contained in the Zinc-Galvanized Steel (ZGS) have a polygonal shape, which was also observed in this work. The hardness is lower in DUPLEX STAINLESS STEEL2205steel, gradually increases as the ZTA advances it, reaches its maximum point in the weld metal close to the SS316LGr50 steel, and gradually decreases as it moves away from the weld metal passing through the Heat-Affected Zone (HAZ), but the final value is higher than the initial one because the microstructure of SS316LGr50 steel has a smaller average diameter compared to DUPLEX STAINLESS STEEL2205.

A box-plot graph was made with the Vickers hardness data, grouped into 10 series, each presenting the cases' data. It is observed that the hardness is intrinsically related to grain size, directly influencing mechanical strength and ductility. It can be seen that the microstructures with the largest average grain size, showed lower hardness. Considering that the welding energy affected the average grain size and its nonuniformity, Figure10 shows that the cases with the lower welding energy obtained higher hardness values and dispersions

In the tensile strength test, all cases 1 and 3 specimens broke at the weld interface with the DSS2205 base metal. The remaining specimens broke into the DSS2205 base metal, keeping the welded region intact. Thus, the tensile strength test eliminated cases 1 and 3 to verify the response to electrochemical corrosion, as they represent an experimental area that is not valid for practical application. The maximum stress results obtained in the test are described in Table7.

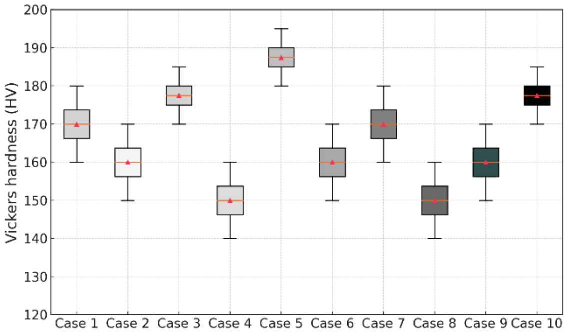

Figure 10. Box Plot of the hardness grouped in the cases

Table 7. Maximum stresses and rupture location.

Case	Va (m/min)	APB	FC	Maximum Tension (MPa)	Standard Deviation (MPa)
1	3.6	-9	1.1	370.5	75.0
2	4.9	-9	1.1	498.8	1.0
3	3.6	9	1.1	290.0	103.5
4	4.9	9	1.1	498.2	9.0
5	3.6	-9	1.6	506.0	2.0
6	4.9	-9	1.6	494.0	5.1
7	3.6	9	1.6	495.5	4.0
8	4.9	9	1.6	498.5	7.0
9	4.3	0	1.3	480.0	14.0
10	4.3	0	1.3	501.5	13.0

The evaluation of electrochemical corrosion did not show significant correlations in this experimental design, even though the literature relates grain size to corrosion tendency. However, the values obtained show statistically significant differences, with 95% certainty. Thus, it is important to consider the corrosion rate obtained with different parameters when optimizing the process. Table 8 with the experimental results and Figure11 are presented below, which easily show the differences of each experimental point.

Table 8. Corrosion rate results in each case.

Case	Corrosion Rate (mpy)	Standard Deviation (mpy)
2	11.925	1.105
4	18.141	0.956
5	11.208	1.012
6	8.556	0.899
7	5.95	0.566
8	7.823	0.945
9	9.224	1.101
10	10.079	1.085

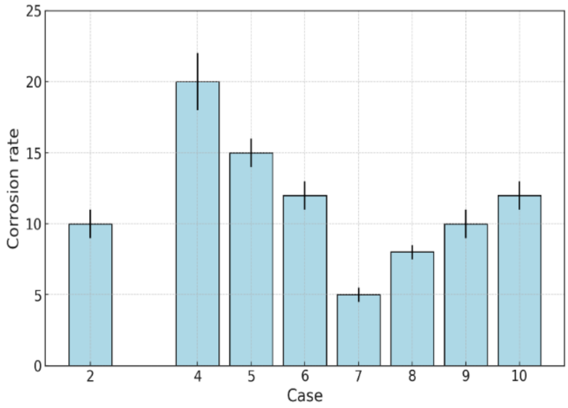

Figure 11. Corrosion rate in each case.

3.1. *Response Surface Methodology (RSM) and Analysis of Variance (ANOVA)*

Response Surface Methodology (RSM) was employed to investigate the effects of key welding parameters, specifically wire feed rate(Va), peak-to-base amplitude (APB), and arc focus (FC), on the welding energy (EJ/mm). The aim was to develop a predictive model that describes the relationship between these parameters and the resulting welding energy, which is a critical factor in determining the weld quality. The RSM is a robust statistical technique that facilitates the modelling and analyzing problems in which several variables influence a response of interest. The objective is to optimize this response. A second-order polynomial model was chosen to capture the potential nonlinear relationships between the welding parameters and energy. The general form of the second-order model used in this analysis is given by Equation(10):

$$\begin{aligned} E_{J/mm} = \beta_0 + \beta_1 \mathrm{Va} + \beta_2 \mathrm{APB} + \beta_3 \mathrm{FC} + \beta_{11} \mathrm{Va}^2 \\ + \beta_{22} \mathrm{APB}^2 + \beta_{33} \mathrm{FC}^2 \\ + \beta_{12} \mathrm{Va} \times \mathrm{APB} + \beta_{13} \mathrm{Va} \\ \times \mathrm{FC} + \beta_{23} \mathrm{APB} \times \mathrm{FC} + (\epsilon) \end{aligned} \quad (10)$$

In this Equation, (β_0) represents the intercept, while $(\beta_1), (\beta_2), and (\beta_3)$ are the linear coefficients of each input factor (Va, APB, and FC). The quadratic terms $(\beta_{11}), (\beta_{22}), and (\beta_{33})$ account for the curvature in the response surface, and the interaction terms $(\beta_{12}), (\beta_{13}), and (\beta_{23})$ explore the combined effects of pairs of factors. The term (ϵ) represents the residual error, capturing the variation in the response that the model cannot explain. After fitting the model to the experimental data, an Analysis of Variance (ANOVA) was conducted to evaluate each factor's significance and interactions statistically. ANOVA helps determine which factors have a statistically significant impact on the response variable, in this case, the welding energy. The results of the ANOVA for the RSM model are presented in Table9.

Table 9. Results of the ANOVA for the RSM model

Factor	Sum of Squares	df	F-value	p-value
Va	44822.981	1	102.865	0.0096
APB	6256.330	1	14.358	0.0631
FC	216456.818	1	496.750	0.0020
Va^2	1290.341	1	2.961	0.2274
APB^2	298.589	1	0.685	0.4948
FC^2	20.831	1	0.048	0.8472
Va	1622.221	1	3.723	0.1934
Va	1340.584	1	3.077	0.2215
APB	473.704	1	1.087	0.4066
Residual	871.492	2		

The ANOVA results reveal that the wire feed speed (Va) and arc focus (FC) have statistically significant effects on the welding energy, as indicated by their p-values of 0.0096 and 0.0020, respectively. The F-values for Va (102.865) and FC (496.750) are considerably high, reinforcing their importance in the model. These results suggest that variations in Va and FC can lead to substantial changes in the welding energy, highlighting their critical roles in the welding process. The peak-to-base amplitude (APB), while showing some influence, is less significant with a p-value of 0.0631, which is close to the conventional threshold for significance ($p < 0.05$). This indicates that APB moderates the welding energy, though it is not as impactful as Va and FC.

The quadratic terms (Va^2, APB^2, FC^2) and interaction terms (Va:APB, Va:FC, APB:FC) were statistically insignificant (p-values > 0.05), indicating that the effects of the welding parameters on welding energy are predominantly linear within the experimental range tested. This supports the conclusion that, on average, the influence of each factor operates independently, without significant interactions driving the response. However, the surface plot in Figure 12 illustrates a nuanced trend: when

Va and FC are both at higher levels, there is an observable amplification in welding energy. This apparent "interaction" arises from the cumulative linear effects of both parameters rather than from a statistically significant interaction term. For example, suppose FC increases while Va remains low. In that case, the contribution to welding energy will reflect the isolated effect of FC, resulting in a lower overall energy increase compared to scenarios where both parameters are high. This indicates that, although the parameters' effects are primarily independent, their combined influence can still result in synergistic outcomes due to additive linear contributions. The independence noted in the statistical analysis pertains to the lack of significant non-linear or interaction effects across the tested range. The combined impact of Va and FC observed in the plots aligns with the additive linear contributions of each factor. This behavior underscores the importance of optimizing both parameters simultaneously to achieve energy efficiency and improved weld quality.

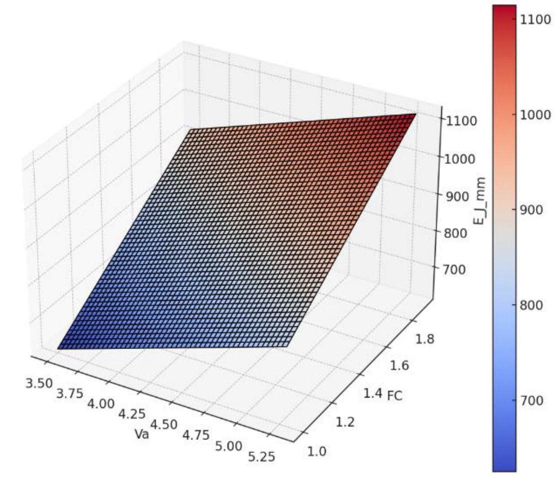

Figure12. 3D Surface Plot of Welding Energy as a function of Va and FC.

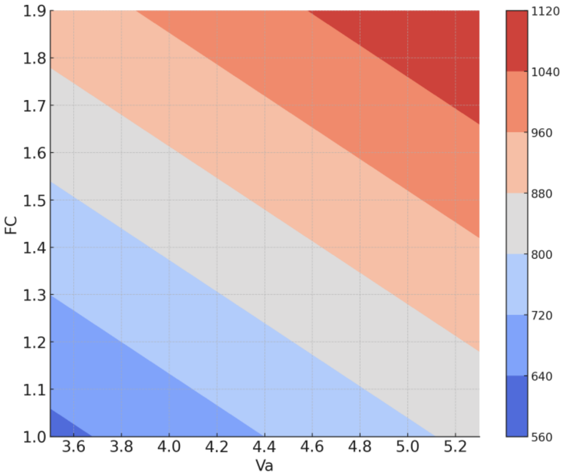

Figure13. Contour Plot of Welding Energy.

The contour plot (Figure13) provides a 2D perspective, making identifying regions of optimal parameter settings easier. The contours indicate that the welding energy is maximized at higher values of both Va and FC, while lower values of these factors correspond to reduced energy levels. These visualizations are crucial for practical applications, as they guide the selection of parameter combinations to achieve the desired welding energy, enhancing the overall welding process.

The RSM analysis combined with ANOVA has successfully identified wire feed rate(Va) and arc focus (FC) as the most influential parameters affecting welding energy. These findings underscore the importance of careful control and optimization of these parameters in industrial welding processes. The insights gained from the 3D surface and contour plots further support the conclusion that higher levels of Va and FC are conducive to achieving optimal welding energy, which is essential for producing high-quality welds.

The results of this analysis provide a valuable foundation for future work, where further refinement of the model could include additional factors or consider more complex interactions, depending on the specific requirements of the welding application.

4. Conclusions

Gas Metal Arc Welding (GMAW) parameters were optimized to improve the mechanical properties and corrosion resistance of dissimilar welds between Duplex Stainless Steel 2205 (DSS2205) and SS316L. A full factorial experimental design and advanced statistical analyses were employed, including ANOVA and Response Surface Methodology (RSM). Optimal welding conditions were achieved at a welding energy of 775 J/mm, producing refined microstructures, superior weld quality, and tensile strength of 506 MPa. The corrosion resistance was significantly enhanced, with the lowest corrosion rate observed at 5.95 mph, attributed to controlled microstructural refinement and reduced intermetallic compound formation. High welding energies increased bead leg lengths but reduced throat dimensions, whereas low energies compromised bead uniformity.

The cruciform joint configuration proved effective for evaluating multidirectional stress responses and real-world applications of welded connections. Findings demonstrated that arc focus and wire feed speed had the most significant impact on weld energy, while the peak-to-base amplitude exhibited moderate effects. These insights provide a robust framework for optimizing dissimilar welds, ensuring a balance between cost and performance.

Further research should explore the long-term durability of these welds under varying environmental and mechanical conditions. Investigating additional welding techniques or hybrid methods could provide further insights into improving weld efficiency and minimizing defects in dissimilar metal joining.

Funding Declaration:

No funding was obtained for this research

Data Availability

The data supporting this findings are available from the corresponding author upon reasonable request.

Conflict of Interest:

The authors declare that no competing financial interests or personal relationships exist that could have appeared to influence the work reported in this paper.

References

[1] M. M. Z. Ahmed, M. M. El-Sayed Seleman, D. Fydrych, and G. ÇAM, “Review on friction stir welding of dissimilar magnesium and aluminum alloys: Scientometric analysis and strategies for achieving high-quality joints,” *Journal of Magnesium and Alloys*, vol. 11, no. 11, 2023, pp. 4082–4127, doi: 10.1016/J.JMA.2023.09.039.

[2] S. Ambade *et al.*, “Experimental investigation of microstructural, mechanical and corrosion properties of 316L and 202 austenitic stainless steel joints using cold metal transfer welding,” *Journal of Materials Research and Technology*, vol. 27, no. 2023, pp. 5881–5888, doi: 10.1016/j.jmrt.2023.11.091.

[3] R. K. Aninda, S. M. Karobi, R. Shariar, Md. M. Rahman, and M. I. I. Rabby, “Effect of post-weld heat treatment on mechanical properties and microstructure in electric arc welded mild steel joints,” *Journal of Engineering Research*, no. 2023, doi: 10.1016/j.jer.2023.10.012.

[4] H. Atapek, M. Tümer, E. Çelikkol, A. Kısasöz, and M. Z. Kerimak, “Microstructural, mechanical and corrosion behavior of UNS S31803/Hastelloy C-276 dissimilar metal welds,” *CIRP J Manuf Sci Technol*, vol. 40, no. 2023, pp. 129–141, doi: 10.1016/j.cirpj.2022.11.008.

[5] F. Badkoobeh, H. Mostaan, F. Nematzadeh, and M. Roshanai, “Nd: YAG laser beam welding of UNS N07718 superalloy and UNS S32304 duplex stainless steel: Phase transformations and mechanical properties of dissimilar joints,” *Opt Laser Technol*, vol. 170, no. 2024, doi: 10.1016/j.optlastec.2023.110254.

[6] O. B. Bembalge, B. Singh, and S. K. Panigrahi, “Magnetic pulse welding of AA6061 and AISI 1020 steel tubes: Numerical and experimental investigation,” *J Manuf Process*, vol. 101, no. 2023, pp. 128–140, doi: 10.1016/j.jmapro.2023.05.098.

[7] V. Bhanu, A. Gupta, and C. Pandey, “Investigation on joining P91 steel and Incoloy 800HT through gas tungsten arc welding for Advanced Ultra Super Critical (AUSC) power plants,” *J Manuf Process*, vol. 80, no. 2022, pp. 558–580, doi: 10.1016/j.jmapro.2022.06.029.

[8] L. Dong, Z. Shi, Y. Zhang, S. Wang, Q. Wang, and L. Liu, “Microstructure and sulfide stress corrosion cracking of the Inconel 625/X80 weld overlay fabricated by cold metal transfer process,” *Int J Hydrogen Energy*, vol. 47, no. 67, 2022, pp. 29113–29130, doi: 10.1016/j.ijhydene.2022.06.210.

[9] S. Agarwal, S. Chakraborty, K. Prasad, and S. Chakraborty, “A Rough Multi-Attributive Border Approximation Area Comparison Approach for Arc Welding Robot Selection,” *Jordan Journal of Mechanical and Industrial Engineering*, vol. 15, no. 2, 2021, pp. 169–180.

[10] S. Dwivedi and S. Sharma, “Optimization of resistance spot welding process parameters on shear tensile strength of SAE 1010 steel sheets joint using Box-Behnken design,” *Jordan Journal of Mechanical and Industrial Engineering*, vol. 10, no. 2, 2016, pp. 115–122.

[11] V. Kumar, “Modeling of weld bead geometry and shape relationships in submerged arc welding using developed fluxes,” *Jordan Journal of Mechanical and Industrial Engineering*, vol. 5, no. 5, 2011, pp. 461–470.

[12] D. Mahto and A. Kumar, “Novel Method of Productivity Improvement and Waste Reduction Through Recycling of Submerged Arc Welding Slag,” *Jordan Journal of Mechanical and Industrial Engineering*, vol. 4, no. 4, 2010, pp. 451–466.

[13] S. A. Rizvi and S. P. Tewari, “Optimization of welding parameters by using Taguchi method and study of fracture mode characterization of SS304H welded by GMA welding,” *Jordan Journal of Mechanical and Industrial Engineering*, vol. 12, no. 1, 2018, pp. 17–22.

[14] A. Sahoo, S. Tripathy, and D. K. Tripathy, “Parametric Optimization of Pulse TIG Welding Process during Joining of Dissimilar Tensile Steels Used in Automotive Industries,” *Jordan Journal of Mechanical and Industrial Engineering*, vol. 16, no. 5, 2022, pp. 663–676.

[15] B. Zhao, “Multi-Layer and Multi-Channel Welding Trajectory Control Method of Welding Robot,” *Jordan Journal of Mechanical and Industrial Engineering*, vol. 16, no. 1, 2022, pp. 153–162.

[16] T. Hassel *et al.*, “Investigation of the mechanical properties and corrosion behaviour of hybrid L 80 Type 1 and duplex steel joints produced by magnetically impelled arc butt welding,” *Journal of Advanced Joining Processes*, vol. 5, no. 2022, doi: 10.1016/j.jajp.2022.100109.

[17] S. Kantur, G. İrsel, and B. N. Güzey, “Investigation of combining the 304L and S355J2C+N materials with TIG welding in terms of microstructure and mechanical properties,” *International Journal of Pressure Vessels and Piping*, vol. 206, no. 2023, doi: 10.1016/j.ijpvp.2023.104999.

[18] H. J. Kim *et al.*, “Process optimization and thermodynamic modeling of weld zone in nickel powder-added dissimilar pulsed-laser NiTi/ASS joint,” *Journal of Materials Research and Technology*, vol. 20, no. 2022, pp. 4197–4212, doi: 10.1016/j.jmrt.2022.08.086.

[19] J. R. Li *et al.*, “Effect of filling materials on microstructure and properties of CMT-laser beam oscillation hybrid welding behavior of dissimilar Al–Mg–Si alloys,” *Journal of Materials Research and Technology*, vol. 26, no. 2023, pp. 8272–8288, doi: 10.1016/j.jmrt.2023.09.132.

[20] S. Li, X. Hou, X. Wang, Z. Liu, Y. Xia, and H. Dong, “Weldability of high entropy alloys: Microstructure, mechanical property, and corrosion resistance,” *J Manuf Process*, vol. 99, no. 2023, pp. 209–229, doi: 10.1016/j.jmapro.2023.05.049.

[21] Y. Tao, Y. Liu, Y. Liu, H. Ren, J. Zhao, and Q. Sun, “A novel approach to optimize weld formation and regulate interfacial microstructure in TC4/304SS dissimilar arc welding by active hybrid shielding gas,” *Journal of Materials Research and Technology*, vol. 25, no. 2023, pp. 1193–1207, doi: 10.1016/j.jmrt.2023.06.011.

[22] X. Luo *et al.*, “Spatiotemporal variations of creep damage in dissimilar welded joints,” *Eng Fract Mech*, vol. 295, no. 2024, p. 109755, doi: 10.1016/J.ENGFRACMECH.2023.109755.

[23] Y. Meng, J. Fu, M. Gong, S. Zhang, M. Gao, and H. Chen, “Laser dissimilar welding of Al/Mg lap-joint with Ti interlayer through optimized 8-shaped beam oscillation,” *Opt Laser Technol*, vol. 162, no. 2023, doi: 10.1016/j.optlastec.2023.109304.

[24] G. Mou *et al.*, “Fabrication of TA2–304 SS laminated metal composite using directed energy deposition-arc: Microstructure, mechanical property, and corrosion resistance,” *Mater Charact*, vol. 207, no. 2024, p. 113529, doi: 10.1016/J.MATCHAR.2023.113529.

[25] N. M. R. Nik Mohamed Daud *et al.*, “Benchmarking the impact of nickel filler addition, weld hardness, environmental pH, and corrosion inhibitors on A333 carbon steel pipe weld corrosion,” *Results in Engineering*, vol. 20, no. 2023, p. 101633, doi: 10.1016/J.RINENG.2023.101633.

[26] A. K. Peethala, B. N. D, S. Rao. K, and R. G, “Optimization of welding parameters and study on mechanical and pitting corrosion behavior of dissimilar stainless steel GTA welds,” *Chemical Data Collections*, vol. 43, no. 2023, doi: 10.1016/j.cdc.2022.100978.

[27] M. Sabzi, S. H. Mousavi Anijdan, A. R. B. Chalandar, N. Park, H. R. Jafarian, and A. R. Eivani, “An experimental investigation on the effect of gas tungsten arc welding current

modes upon the microstructure, mechanical, and fractography properties of welded joints of two grades of AISI 316L and AISI310S alloy metal sheets," *Materials Science and Engineering: A*, vol. 840, no. 2022, doi: 10.1016/j.msea.2022.142877.

[28] P. Singh, N. Arora, and A. Sharma, "Enhancing mechanical properties and creep performance of 304H and inconel 617 superalloy dissimilar welds for Advanced Ultra Super Critical power plants," *International Journal of Pressure Vessels and Piping*, vol. 201, no. 2023, doi: 10.1016/j.ijpvp.2022.104882.

[29] S. Tokita, C. Y. Liu, and Y. S. Sato, "Effects of material combination for ultrasonic spot welding on microstructure and strength of Al/Al, Al/Cu, and Al/Ni dissimilar joints," *Journal of Materials Research and Technology*, vol. 26, no. 2023, pp. 7619–7633, doi: 10.1016/j.jmrt.2023.09.094.

[30] P. Xiao *et al.*, "Effect of wire composition on microstructure and penetration crack of laser-cold metal transfer hybrid welded Cu and stainless steel joints," *Mater Chem Phys*, vol. 299, no. 2023, doi: 10.1016/j.matchemphys.2023.127480.

[31] D. S. Yu, Y. Zhang, J. P. Zhou, D. Q. Sun, and H. M. Li, "Effect of process parameters on interface microstructure and performance in laser welding of steel-ZrO2 ceramic," *Ceram Int*, vol. 49, no. 23, 2023, pp. 39532–39558, doi: 10.1016/j.ceramint.2023.09.305.

[32] V. Bhanu, S. M. Pandey, A. Gupta, and C. Pandey, "Dissimilar weldments of P91 and Incoloy 800HT: Microstructure, mechanical properties, and residual stresses," *International Journal of Pressure Vessels and Piping*, vol. 199, no. 2022, doi: 10.1016/j.ijpvp.2022.104782.

[33] S. Kumar Maurya *et al.*, "Welding studies on dissimilar magnesium alloys for improving corrosion behaviour," *Mater Today Proc*, vol. 63, no. 2022, pp. 623–629, doi: 10.1016/j.matpr.2022.04.378.

[34] A. K. Maurya, C. Pandey, and R. Chhibber, "Dissimilar welding of duplex stainless steel with Ni alloys: A review," *International Journal of Pressure Vessels and Piping*, vol. 192, no. 2021, doi: 10.1016/j.ijpvp.2021.104439.

[35] H. Vardhan Thigulla, V. Pranay Kumar, G. Teja Yadav, and B. Challa, "Experimental investigation and optimization of Aluminium 6061 by using various welding process – A review," *Mater Today Proc*, no. 2023, doi: 10.1016/j.matpr.2023.10.097.

[36] B. R. Moharana, S. K. Sahoo, D. K. Biswal, and K. Muduli, "Influence of fusion welding processes on microstructure and mechanical properties of dissimilar metal (AISI 304 SS-Copper) weldment," *Mater Today Proc*, no. 2023, doi: 10.1016/j.matpr.2023.10.135.

[37] F. Liu *et al.*, "Melt flowing behaviors and microstructure evolution during laser offset welding of dissimilar metals between AH36 and 304 steels," *Opt Laser Technol*, vol. 151, no. 2022, doi: 10.1016/j.optlastec.2022.108024.